

Noise reduction via dual-grid charge averaging

Haiyun Tan(谭海云), Tianyuan Huang(黄天源), Peiyu Ji(季佩宇), Liang Xu(徐亮), and Xuemei Wu(吴雪梅)
Citation: Chin. Phys. B, 2026, 35 (**6**): 065201. DOI: 10.1088/1674-1056/ae1018
http://cpb.iphy.ac.cn; http://iopscience.iop.org/cpb

What follows is a list of articles you may be interested in

Accelerating and guiding of electron beams in a cone target filled with near-critical-density plasmas

Jie-Jie Lan(蓝婕婕), Zhang-Hu Hu(胡章虎), and You-Nian Wang(王友年)
Chin. Phys. B, 2025, 34 (**12**): 125201. DOI: 10.1088/1674-1056/adea5b

One-dimensional theoretical analysis on charged-particle transports in a decaying plasma with an initial plasma-electrode gap

Xin-Li Sun(孙鑫礼), Yao-Ting Wang(汪耀庭), Lan-Yue Luo(罗岚月), Zi-Ming Zhang(张子明), Meng-Long Zhang(张梦龙), He-Ping Li(李和平), Dong-Jun Jiang(姜东君), and Ming-Sheng Zhou(周明胜)
Chin. Phys. B, 2025, 34 (**11**): 115201. DOI: 10.1088/1674-1056/ade385

Pulse interval tunable terahertz radiation from electron beam-plasma interactions

Die Jian(简蝶), Jie Cai(蔡杰), Li-Qi Han(韩立琦), Xing-Yu Zhao(赵兴宇), Han Wen(温寒), and Jin-Qing Yu(余金清)
Chin. Phys. B, 2025, 34 (**10**): 105201. DOI: 10.1088/1674-1056/add67a

Influence of grid on the extraction characteristics of different charged ions in mixed ion beams

Ao Xu(徐翱), Xiang Wan(万翔), and Pingping Gan(甘娉娉)
Chin. Phys. B, 2025, 34 (**8**): 085202. DOI: 10.1088/1674-1056/add4e0

Influence of ion species on extraction characteristics of mixed ion beams

Ao Xu(徐翱), Pingping Gan(甘娉娉), Xiang Wan(万翔), and Yuanjie Shi(石元杰)
Chin. Phys. B, 2024, 33 (**9**): 095202. DOI: 10.1088/1674-1056/ad5c3d

---

Noise reduction via dual-grid charge averaging

Haiyun Tan(谭海云)[1,2,3], Tianyuan Huang(黄天源)[2,3], Peiyu Ji(季佩宇)[4], Liang Xu(徐亮)[2,3,†], and Xuemei Wu(吴雪梅)[2,3,‡]

[1] *School of Electronic Information Engineering, Suzhou Polytechnic University, Suzhou* 215000, *China*

[2] *School of Physical Science and Technology & Collaborative Innovation Center of Suzhou Nano Science and Technology, Soochow University, Suzhou* 215006, *China*

[3] *Key Laboratory of Advanced Optical Manufacturing Technologies of Jiangsu Province & Key Laboratory of Modern Optical Technologies of Education Ministry of China, Soochow University, Suzhou* 215006, *China*

[4] *School of Microelectronics and School of Integrated Circuits, Nantong University, Nantong* 226019, *China*

(Received 10 July 2025; revised manuscript received 19 September 2025; accepted manuscript online 7 October 2025)

Numerical heating in particle-in-cell simulations arises primarily from statistical noise during the deposition process, which has long been a critical bottleneck limiting long-term simulation accuracy. This work proposes a dual-grid scheme that enhances sampling accuracy by leveraging complementary spatial information from two staggered grids, thereby reducing statistical noise. Analytical derivations show that, through its distinctive deposition mechanism, the scheme effectively elevates bilinear interpolation to a higher-order formulation. Numerical experiments validate this conclusion: compared to quadratic interpolation, the proposed method achieves comparable noise suppression and mitigation of noise-driven heating, while exhibiting superior capability in controlling grid heating and preserving energy conservation in long-term simulations. Most importantly, phase-space diagnostics confirm that the scheme delivers the highest simulation accuracy among the tested methods. These results demonstrate that the proposed approach provides an effective pathway for advancing noise control in particle-in-cell simulations.

Keywords: particle-in-cell, numerical noise, finite-grid-instability

PACS: 52.80.Pi, 52.27.Aj, 52.65.Rr

DOI: 10.1088/1674-1056/ae1018 **CSTR:** 32038.14.CPB.ae1018

1. Introduction

Particle-in-cell (PIC) simulations have long served as a cornerstone methodology in plasma physics, enabling detailed exploration of fundamental processes such as wave–particle coupling,[1] relativistic laser–plasma interactions,[2] magnetospheric reconnection,[3] and plasma–surface interactions in industrial applications.[4] Despite their wide applicability, a persistent challenge in PIC simulations is the phenomenon of numerical heating,[5–9] as it can obscure physical effects and compromise long-term accuracy. For example, in high-energy-density laser–plasma studies, artificial energy inflation exceeding 25% has been observed after only 1 ps of simulation time,[10] under conditions with an initial plasma density of $n_e = 1.11 \times 10^{23}$ cm^{-3}, initial electron temperature $T_e = 1$ keV, grid spacing $\Delta x = 1.5c/\omega_p$, 64 macroparticles per cell, and the use of a top-hat shape function.

It is widely recognized that numerical heating primarily arises from non-conservative forces associated with the discontinuous deposition of charge/current onto discrete grids when sampling is insufficient.[11] The combined effects of grid discretization and a finite number of macroparticles inevitably introduce two distinct error contributions in the estimation of charge and current densities: (i) grid-induced error, of which the aliasing error is a significant component, resulting from finite spatial resolution, and (ii) sampling error, often referred to as statistical noise, which scales as $1/\sqrt{N_p}$ for N_p macroparticles.[12–16] Both types of error seed unphysical fields that feedback on particles and drive artificial energy growth; their relative importance depends on simulation parameters such as Δx, N_p, and the deposition scheme. In most practical PIC simulations, statistical noise is the dominant noise source.

A range of methods have been proposed to mitigate noise, such as high-order particle shape functions,[17,18] digital filtering,[19] stochastic resampling and remapping,[20] and sparse grid techniques.[21–24] However, each approach entails trade-offs: filters may attenuate legitimate high-frequency physics, resampling schemes can be mathematically and computationally complex, and sparse-grid methods can struggle to resolve strongly localized structures.[14] High-order shape functions (*e.g.*, quadratic B-splines) are often effective and robust in reducing numerical heating,[10] but they mainly act by smoothing the interpolation kernel and do not explicitly target the fundamental statistical origin of noise.

We contend that effective noise suppression must directly address the underlying error mechanisms rather than relying

†Corresponding author. E-mail: liangxu@suda.edu.cn

‡Corresponding author. E-mail: xmwu@suda.edu.cn

© 2026 Chinese Physical Society and IOP Publishing Ltd. All rights, including for text and data mining, AI training, and similar technologies, are reserved.

solely on the enhanced interpolation smoothness. Sparse-grid methods exemplify this philosophy by improving sampling efficiency.[25] Motivated by this perspective, the present work introduces a dual-grid charge averaging scheme, designed to mitigate statistical noise arising from insufficient particle sampling. By leveraging complementary spatial information from two staggered grids, the proposed method enhances sampling accuracy and reduces statistical noise. Interestingly, this approach can also mitigate aliasing error.

The remainder of this paper is organized as follows. Section 2 reviews the conventional single-grid charge deposition scheme and details the formulation of the dual-grid charge averaging method, including the derivation of its equivalent shape function and a theoretical estimate of its noise-reduction capability. Section 3 reports a series of numerical experiments comparing the proposed method with bilinear and quadratic interpolation, focusing on noise robustness, energy conservation, and overall simulation fidelity. Finally, Section 4 summarizes the main findings and outlines the implications of this work.

2. Methodology

This section begins by addressing strategies aimed at mitigating statistical noise arising from the finite number of macroparticles (hereinafter referred to as particles), which typically constitutes the dominant source of noise in most PIC simulations. Following an overview of potential approaches for reducing statistical noise, the discussion will then turn to grid-induced error, which represents an additional critical factor governing the accuracy and stability of long-term simulations.

2.1. Statistical noise estimation

In PIC algorithms, the charge density contributed by particles is deposited onto a fixed set of grid points. The deposition onto adjacent grid points is carried out according to the following expression:[6]

$$\rho\left(\boldsymbol{x}_g\right)=\sum_{s_\mathrm{p}}\sum_{n=1}^{N_\mathrm{p}} q_\mathrm{p} S\left(\boldsymbol{x}_g-\boldsymbol{x}_\mathrm{p}^n\right), \tag{1}$$

where $\boldsymbol{x}_g$ denotes the position of the adjacent grid points. The quantities s_p, q_p, N_p, and $\boldsymbol{x}_\mathrm{p}$ represent the particle species, charge, number, and position, respectively. $S(x)$ is the particle shape function, which in this case corresponds to the widely used bilinear interpolation, defined as follows:[26]

$$S(x)=\frac{1}{\Delta x}\max\left\{0,1-\frac{|x|}{\Delta x}\right\}. \tag{2}$$

Considering an infinite one-dimensional (1D) uniform plasma slab, we restrict attention to a finite region of length L. For simplicity, only a single particle, labeled as 'p', is assumed to reside within this region. By repeatedly sampling this particle from the plasma distribution function a total of N times, one obtains N particle positions together with N corresponding charge densities deposited at a given grid point 'g', expressed as follows:

$$x_\mathrm{p}=\left\{x_\mathrm{p}^1,x_\mathrm{p}^2,x_\mathrm{p}^3,\ldots,x_\mathrm{p}^{N-1},x_\mathrm{p}^N\right\}, \tag{3a}$$

$$\rho\left(x_g\right)=\left\{\rho_g^1,\rho_g^2,\rho_g^3,\ldots,\rho_g^{N-1},\rho_g^N\right\}. \tag{3b}$$

The statistical noise σ_n is defined as the standard deviation of ρ_g[21]

$$\begin{aligned}\left(\sigma_\mathrm{n}\right)^2 &= \frac{1}{N}\sum_{n=1}^{N}\left[\rho_g^n-\bar{\rho}\left(x_g\right)\right]^2\\ &= \mathbb{E}[\rho^2]-(\bar{\rho})^2,\end{aligned} \tag{4}$$

where $\mathbb{E}[X]$ represents the mathematical expectation of X. We have used ρ to represent $\rho(x_g)$.

First compute $\bar{\rho}$:

$$\begin{aligned}\bar{\rho} &= \frac{1}{N}\sum_{n=1}^{N} q_\mathrm{p} S\left(x_g-x_\mathrm{p}^n\right)\\ &= q_\mathrm{p} E\left[S\left(x_g-x_\mathrm{p}^n\right)\right]\\ &= q_\mathrm{p}\frac{1}{L}\int_0^L S\left(x_g-x_\mathrm{p}\right)\mathrm{d}x_\mathrm{p}\\ &= q_\mathrm{p}/L.\end{aligned} \tag{5}$$

In Eq. (5), we have assumed that $N\to\infty$, so the discrete summation is approximated as an integral.

Then compute $\mathbb{E}[\rho^2]$:

$$\begin{aligned}\mathbb{E}[\rho^2] &= \left(q_\mathrm{p}\right)^2\frac{1}{N}\sum_{n=1}^{N}\left[S\left(x_g-x_\mathrm{p}^n\right)\right]^2\\ &= \left(q_\mathrm{p}\right)^2 E\left[S\left(x_g-x_\mathrm{p}^n\right)^2\right]\\ &= \left(q_\mathrm{p}\right)^2\frac{1}{L}\int_0^L S\left(x_g-x_\mathrm{p}^n\right)^2\mathrm{d}x_\mathrm{p}\\ &= \left(q_\mathrm{p}\right)^2\frac{1}{L}\frac{1}{2\pi}\int\left|\tilde{S}(k)\right|^2\mathrm{d}k.\end{aligned} \tag{6}$$

The last step in Eq. (6) is to transform the integration space from the real domain to the frequency domain. The Fourier transform of the m-order shape function is expressed as follows:[6]

$$\tilde{S}_m(k)=\left[\mathrm{sinc}\left(\frac{k\Delta x}{2}\right)\right]^{m+1}. \tag{7}$$

Substituting Eq. (7) into Eq. (6) yields

$$\mathbb{E}[\rho^2]=\left(q_\mathrm{p}\right)^2\frac{1}{L}\frac{1}{2\pi}\int\left[\mathrm{sinc}\left(\frac{k\Delta x}{2}\right)\right]^{2(m+1)}\mathrm{d}k. \tag{8}$$

Taking $m=1$ (corresponding to bilinear interpolation), one gets $\mathbb{E}\left[\rho^2\right]=\frac{2}{3}\frac{1}{L\Delta x}\left(q_\mathrm{p}\right)^2$. Therefore, the statistical noise is $(m=1)$

$$\left(\sigma_{n\#1}\right)^2 = \frac{2}{3}\frac{1}{L\Delta x}\left(q_\mathrm{p}\right)^2-\left(\frac{q_\mathrm{p}}{L}\right)^2$$

$$= \left(\frac{2}{3}\frac{q_\mathrm{p}}{\Delta x} - \frac{q_\mathrm{p}}{L}\right)\frac{q_\mathrm{p}}{L}$$
$$\approx \frac{2}{3}\frac{q_\mathrm{p}}{\Delta x}\bar{\rho}, \tag{9}$$

which is consistent with the derivation results of Muralikrishnan *et al.*[21] For quadratic interpolation ($m=2$), the statistical noise is $(\sigma_{n\#2})^2 = 0.55\frac{q_\mathrm{p}}{\Delta x}\bar{\rho}$.

2.2. Reduction technique

In conventional deposition schemes, the statistical estimation of $\rho(x_g)$ is determined solely by the charge contributions deposited directly by particles onto the grid point 'g'. To improve the accuracy of this estimation, we propose a novel scheme that incorporates statistical information from multiple sampling locations, including both integer and half-integer grid points. By integrating contributions from these complementary sampling positions, the method facilitates mutual error compensation and thereby reduces the variance inherent in single-point estimations on a fixed computational grid.

The proposed implementation is realized through the mapping and averaging of spatial grid points. Revisiting the plasma slab model, we define two independent sets of charge densities as follows.

(i) Native group:

$$\rho_{\#1}(x_g) = \left\{\rho_g^1, \rho_g^2, \ldots, \rho_g^N\right\}, \tag{10}$$

which is obtained by depositing particles directly onto the integer grid point g, as described in Eq. (3b).

(ii) Mapped group:

$$\rho_{\#2}(x_g) = \left\{\rho_{g\#2}^1, \rho_{g\#2}^2, \ldots, \rho_{g\#2}^N\right\}, \tag{11}$$

where each element is defined as

$$\rho_{g\#2}^n = \frac{1}{2}\left(\rho_{g-0.5}^n + \rho_{g+0.5}^n\right). \tag{12}$$

In this case, particles are first deposited onto the half-integer grid points '$g-0.5$' and '$g+0.5$', and the corresponding charge densities are then mapped back to the integer grid point 'g' through midpoint averaging.

The final charge density is obtained by taking the average of the native and mapped groups:

$$\rho(x_g) = \frac{1}{2}[\rho_{\#1}(x_g) + \rho_{\#2}(x_g)]. \tag{13}$$

We refer to this method as the dual–grid charge averaging (DGCA) scheme. The grid operation process is illustrated in Fig. 1, where the rectangle denotes the particle position x_p, while the circle and triangle correspond to the integer and half-integer grid points, respectively. The black, blue, and red boxes represent the standard group, the native group, and the mapped group, respectively.

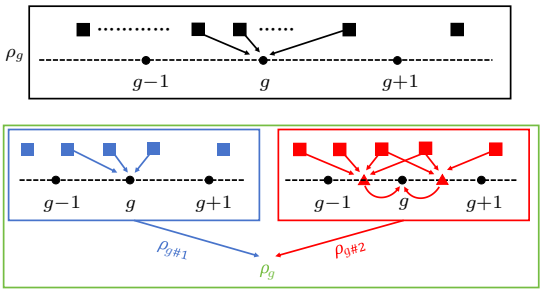


Fig. 1. Algorithm flowchart illustrating operations on integer and half-integer grids. The black box denotes the standard (reference) group. The blue and red boxes represent the native group and the mapped group, respectively.

In this paper, the DGCA scheme is applied to bilinear interpolation in order to derive the corresponding shape function. Let the shape functions defined on the integer and half-integer grids be denoted by $S_\mathrm{f}(x)$ and $S_\mathrm{h}(x)$, respectively. The integer grid points are labeled as $(\cdots,-1,0,1,\cdots)$, while the half-integer grid points are labeled as $(\cdots,-1.5,-0.5,0.5,1.5,\cdots)$. Without loss of generality, the analysis can be restricted to the grid point at '0'. The first step involves mapping the half-integer grid points onto the integer grid points,

$$S_{\mathrm{h}\to\mathrm{f}}(x) = \frac{1}{2}\left[S_\mathrm{h}\left(\boldsymbol{x}_{-0.5}-\boldsymbol{x}_\mathrm{p}\right) + S_\mathrm{h}\left(\boldsymbol{x}_{0.5}-\boldsymbol{x}_\mathrm{p}\right)\right]$$
$$= \frac{1}{\Delta x}\begin{cases}\dfrac{1}{2}, & |x| \le \dfrac{1}{2}\Delta x,\\ \dfrac{3}{4} - \dfrac{1}{2}\dfrac{|x|}{\Delta x}, & \dfrac{1}{2}\Delta x \le |x| \le \dfrac{3}{2}\Delta x,\\ 0, & \text{otherwise},\end{cases} \tag{14}$$

after which the shape function $S_\mathrm{f}(x)$ is written out:

$$S_\mathrm{f}(x) = \frac{1}{\Delta x}\begin{cases}1 - \dfrac{|x|}{\Delta x}, & |x| \le \Delta x,\\ 0, & \text{otherwise}.\end{cases} \tag{15}$$

Finally, the shape function of the DGCA scheme can be obtained as follows:

$$S_\mathrm{D}(x) = \frac{1}{2}\left[S_\mathrm{f}(x) + S_{\mathrm{h}\to\mathrm{f}}(x)\right]$$
$$= \frac{1}{\Delta x}\begin{cases}\dfrac{3}{4} - \dfrac{1}{2}\dfrac{|x|}{\Delta x}, & 0 \le |x| \le \dfrac{1}{2}\Delta x,\\ \dfrac{7}{8} - \dfrac{3}{4}\dfrac{|x|}{\Delta x}, & \dfrac{1}{2}\Delta x \le |x| \le \Delta x,\\ \dfrac{3}{8} - \dfrac{1}{4}\dfrac{|x|}{\Delta x}, & \Delta x \le |x| \le \dfrac{3}{2}\Delta x,\\ 0, & \text{otherwise},\end{cases} \tag{16}$$

which is a four-segment function with a width of $3\Delta x$.

Figure 2(a) presents the functional forms of $S_{\mathrm{h}\to\mathrm{f}}(x)$, $S_\mathrm{f}(x)$, and $S_\mathrm{D}(x)$. Notably, $S_\mathrm{D}(x)$ exhibits a striking resemblance to quadratic interpolation. This is further highlighted in Fig. 2(b), which compares bilinear, quadratic, and DGCA interpolations. The structural similarity indicates that the DGCA scheme effectively mimics higher-order interpolation through its adaptive charge deposition mechanism.

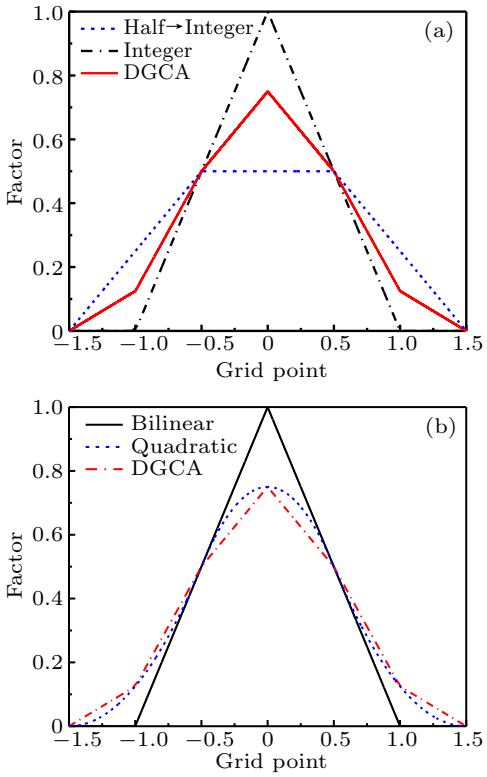


Fig. 2. The function diagrams of different shape functions. (a) The functions $S_{\mathrm{h}\to\mathrm{f}}(x)$, $S_{\mathrm{f}}(x)$, and $S_{\mathrm{D}}(x)$ are represented by blue dashed line, black dotted line, and red solid line, respectively. (b) The bilinear, quadratic and DGCA interpolation are represented by black solid line, blue dashed line, and red dotted line, respectively.

2.3. Noise reduction estimation

Although the DGCA scheme was initially developed with the primary objective of mitigating statistical noise, our analysis first focuses on grid-induced errors before returning to statistical noise. A particularly detrimental consequence of a discrete grid is aliasing, which introduces spurious spectral components and undermines numerical accuracy. Accordingly, the capability of the proposed scheme to reduce grid-induced errors is evaluated by examining its effectiveness in suppressing aliasing.

The Fourier transform of the shape function $S(x)$ is

$$\begin{aligned}\tilde{S}(k) &= \int_{-\infty}^{\infty} S(x)\,\mathrm{e}^{-\mathrm{i}kx}\,\mathrm{d}x \\ &= \int_{-\infty}^{\infty} \{S(x)\times[\cos(kx)-\mathrm{i}\sin(kx)]\}\,\mathrm{d}x. \end{aligned} \tag{17}$$

Since the shape function of the DGCA scheme $S_{\mathrm{D}}(x)$ is an even function, Eq. (17) is rewritten as

$$\begin{aligned}\tilde{S}_{\mathrm{D}}(k) &= 2\int_0^{\infty} S_{\mathrm{D}}(x)\cos(kx)\,\mathrm{d}x \\ &= \frac{0.5\cos\left(\frac{k\Delta x}{2}\right)-\cos(k\Delta x)-0.5\cos\left(\frac{3k\Delta x}{2}\right)+1}{(k\Delta x)^2} \\ &= \frac{1-\cos(k\Delta x)+\sin(k\Delta x)\sin\left(\frac{k\Delta x}{2}\right)}{(k\Delta x)^2} \\ &= \frac{2\sin^2\left(\frac{k\Delta x}{2}\right)\left[1+\cos\left(\frac{k\Delta x}{2}\right)\right]}{(k\Delta x)^2} \\ &= \mathrm{sinc}^2\left(\frac{k\Delta x}{2}\right)\cos^2\left(\frac{k\Delta x}{4}\right). \end{aligned} \tag{18}$$

The third step of Eq. (18) uses the identity $\cos a-\cos b=-2\sin\left(\frac{a+b}{2}\right)\sin\left(\frac{a-b}{2}\right)$, and the fourth step uses the identities $1-\cos(a)=2\sin^2\left(\frac{a}{2}\right)$ and $\sin(a)=2\sin\left(\frac{a}{2}\right)\cos\left(\frac{a}{2}\right)$.

As clearly shown in Eq. (18), the DGCA scheme exhibits a distinct "filtering" characteristic: the $\mathrm{sinc}^2\left(\frac{k\Delta x}{2}\right)$ term serves as the primary mechanism for attenuating high-wavenumber signals, while the additional $\cos^2\left(\frac{k\Delta x}{4}\right)$ term introduces periodic modulation, thereby further suppressing specific high-frequency components and enhancing the overall filtering effectiveness across the high-frequency spectrum.

For a more intuitive comparison, Fig. 3 plots the Fourier response curves of bilinear interpolation $\tilde{S}_1(k)$, quadratic interpolation $\tilde{S}_2(k)$, and the DGCA scheme $\tilde{S}_{\mathrm{D}}(k)$. It is evident that the DGCA scheme achieves stronger attenuation in the high-wavenumber region approaching the Nyquist wavenumber $k_{\mathrm{Ny}}=\pi/\Delta x$, where aliasing is most pronounced. For example, taking $k=\pi/\Delta x$, one obtains $\tilde{S}_1(k)\approx 0.4053$, $\tilde{S}_2(k)\approx 0.2580$, and $\tilde{S}_{\mathrm{D}}(k)\approx 0.2026$.

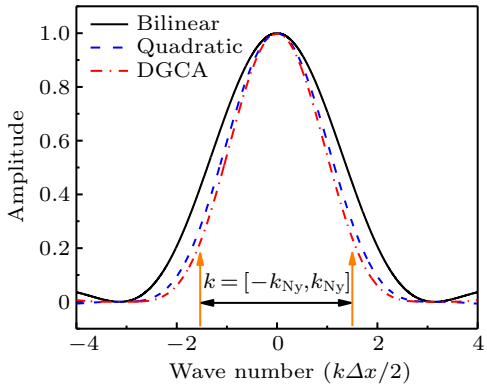


Fig. 3. Fourier transforms of the three shape functions. The bilinear, quadratic and DGCA interpolation are represented by black solid line, blue dashed line and red dotted line, respectively. It can be seen that the DGCA scheme provides better attenuation in the high-wavenumber region near the Nyquist wavenumber $k_{\mathrm{Ny}}=\pi/\Delta x$, where aliasing is most pronounced.

Then evaluate the statistical noise

$$\begin{aligned}(\sigma_{n\#D})^2 &= \mathbb{E}\left[\rho^2\right]-(\bar{\rho})^2 \\ &= (q_{\mathrm{p}})^2\frac{1}{L}\frac{1}{2\pi}\int\left|\tilde{S}_{\mathrm{D}}(k)\right|^2\mathrm{d}k-\left(\frac{q_{\mathrm{p}}}{L}\right)^2 \\ &\approx 0.51 q_{\mathrm{p}}\frac{\bar{\rho}}{\Delta x}. \end{aligned} \tag{19}$$

The coefficients of the statistical noise levels associated with bilinear and quadratic interpolation are given by $\sigma_{n\#1}\sim\sqrt{0.67}$ and $\sigma_{n\#2}\sim\sqrt{0.55}$, respectively. Accordingly, relative to bilinear interpolation, the statistical noise is reduced to 87.5% when using the DGCA scheme and to 90.8% when using quadratic interpolation.

The foregoing analysis demonstrates that the DGCA scheme, by virtue of its unique charge deposition mechanism, effectively upgrades bilinear interpolation to a higher-order

formulation. Although its shape function closely resembles that of quadratic interpolation, DGCA exhibits superior performance in suppressing aliasing. In addition, with respect to statistical noise reduction, DGCA achieves a slight improvement over quadratic interpolation.

3. Numerical experiments

To evaluate the effectiveness of the proposed method, we performed a series of 1D1V electrostatic PIC simulations. The performance of the standard charge deposition scheme was systematically compared against that of the DGCA method under identical simulation conditions. In addition, a comparative analysis with quadratic interpolation was carried out to examine their similarities in noise suppression. The DGCA algorithm was implemented according to Eq. (17). For numerical convenience, the following normalized units were adopted unless otherwise specified: electron Debye length $\lambda_{\mathrm{De}} = 1$, electron plasma frequency $\omega_{\mathrm{pe}} = 1$, and charge-to-mass ratio $q_{\mathrm{e}}/m_{\mathrm{e}} = -1$. The electron thermal velocity was defined through the fundamental relation $v_{\mathrm{the}} = \lambda_{\mathrm{De}}\omega_{\mathrm{pe}}$. To ensure the purity of the numerical results, all filtering operations were deliberately excluded from the simulations to avoid potential artifacts.

3.1. Benchmark test

To validate the reliability of the proposed scheme, we first conducted benchmark tests on two classical plasma physics problems with well-established analytical solutions: Landau damping and the two-stream instability. For the Landau damping case, the initial wave was excited by perturbing particle positions according to $\boldsymbol{x}_{\mathrm{p}} = \boldsymbol{x}_0[1 + 0.05\cos(k\boldsymbol{x}_0)]$, where $\boldsymbol{x}_0$ denotes the equilibrium position and k is the wavenumber. The subsequent temporal evolution of the electric field energy, $E_{\mathrm{f}} = \frac{1}{2}\Delta x\sum E_{\mathrm{g}}^2$, was then monitored and compared with the theoretical damping rate γ_{L} obtained from the dispersion relation[28]

$$1 + \frac{1}{(k\lambda_{\mathrm{De}})^2}\left[1 + \frac{\omega}{kv_{\mathrm{the}}}Z\left(\frac{\omega}{kv_{\mathrm{the}}}\right)\right] = 0, \tag{20}$$

where Z represents the plasma dispersion function and ω denotes the complex wave frequency, $\omega = \mathrm{Re}\,(\omega) + \gamma_{\mathrm{L}}\mathrm{i}$.

In the two-stream instability scenario, we consider counter-propagating electron beams with drift velocities of $\pm u_0$ and a characteristic plasma frequency ω_{pe0}.

This configuration excites electrostatic modes with frequency ω and wavenumber k, which are governed by the dispersion relation[29]

$$\frac{\omega_{\mathrm{pe0}}^2}{(\omega - ku_0)^2} + \frac{\omega_{\mathrm{pe0}}^2}{(\omega + ku_0)^2} = 1. \tag{21}$$

The system supports unstable modes when the condition $ku_0 < \sqrt{2}\omega_{\mathrm{pe0}}$ is satisfied, with the corresponding growth rate given by $\gamma_{\mathrm{T}} = \mathrm{IM}(\omega)$. To selectively excite the most unstable mode, a small-amplitude perturbation was introduced into the initial electron velocity distribution, expressed as $v_{\mathrm{e}} = v_{\mathrm{e0}}[1 + \alpha\cos(kv_{\mathrm{e0}})]$, where $\alpha = 0.005$ denotes the perturbation amplitude.

Figure 4 illustrates the temporal evolution of the electric field energy, with panel (a) corresponding to Landau damping and panel (b) depicting the two-stream instability. Here, the total particle number is 50000 and the other simulation parameters are provided in the figure annotations. The theoretical prediction is indicated by the green curve.

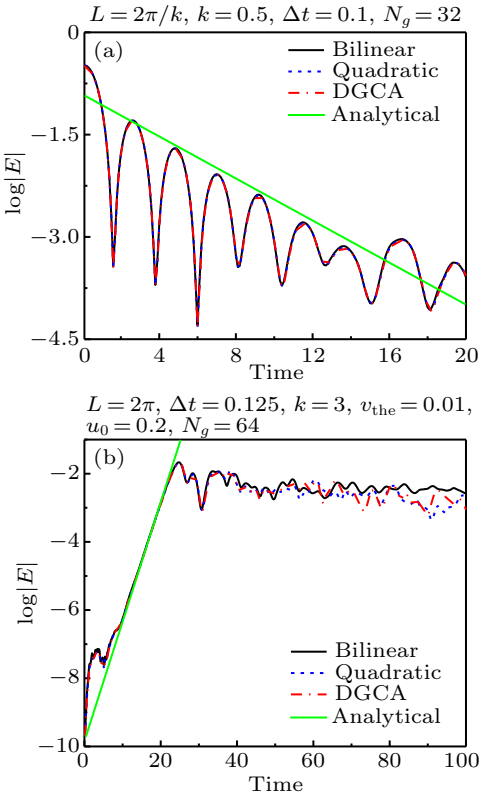


Fig. 4. Time history of total electric field energy in simulating: (a) Landau damping and (b) two-stream instability. The bilinear, quadratic, DGCA interpolation, and analytical result are represented by black solid line, blue dashed line, red dotted line, and green solid line, respectively. The DGCA scheme accurately captures the growth rates.

During the initial phase of Landau damping and the exponential growth stage of the two-stream instability, all three numerical schemes produce growth rates that are in excellent agreement with theoretical predictions. However, in the nonlinear saturation stage of the two-stream instability, the methods exhibit different oscillatory behaviors. These differences highlight the sensitivity of the nonlinear regime to algorithmic implementation and underscore the intrinsic variations among the three deposition schemes.

3.2. Noise reduction test

We further simulated electron motion in a stationary ion background to validate the noise reduction capability of the proposed method. In the initialization phase, electrons were

uniformly distributed in configuration space, while their initial velocity components were sampled from a Maxwellian distribution. As the simulation evolved, the grid charge density ρ_g^n was systematically recorded at each time step n. The level of statistical noise was subsequently quantified at the end of the simulation using the following expression:

$$\mathrm{Var}(\rho_g) = \frac{1}{N_\mathrm{t}} \sum_{n=1}^{N_\mathrm{t}} \left(\rho_g^n - \bar{\rho}_g\right)^2, \tag{22a}$$

$$\bar{\delta}_\mathrm{n} = \frac{1}{N_g} \sum_{g=1}^{N_g} \left[\sqrt{\mathrm{Var}(\rho_g)}\right]. \tag{22b}$$

Here, N_t and N_g denote the total number of time steps and spatial grid points, respectively. $\mathrm{Var}(\rho_g)$ represents the variance of the charge density at the grid points, while $\bar{\delta}_\mathrm{n}$ denotes the average statistical noise.

Figure 5 summarizes the simulation results. Panel (a) illustrates the spatial distribution of $\mathrm{Var}(\rho_g)$, with the dashed line indicating its mean value. Panels (b) and (c) present the dependence of the averaged statistical noise $\bar{\delta}_\mathrm{n}$ on the grid spacing Δx and the number of particles per cell N_c, respectively. Panel (d) compares the relative performance of quadratic interpolation and the DGCA scheme with that of bilinear interpolation, using the data obtained from panel (c). The simulations were conducted with a time step of $\Delta t = 0.2$, a total of $N_g = 64$ cells, and $N_\mathrm{t} = 1000$ time steps. Additional parameters are specified in the corresponding figure caption.

As shown in Fig. 5(a), the DGCA scheme exhibits a pronounced reduction in charge density fluctuations (lower variance) compared with the standard bilinear interpolation. Moreover, its noise suppression capability surpasses that of quadratic interpolation.

At finer grid spacings ($\Delta x \leq 4$), the noise level follows an inverse proportionality to Δx, consistent with the theoretical scaling $\delta_\mathrm{n} \propto \sqrt{1/\Delta x}$, as illustrated in Fig. 5(b). At coarser resolutions ($\Delta x > 4$), however, a clear divergence emerges: while the bilinear interpolation scheme develops oscillatory noise that grows non-monotonically with Δx, both the DGCA and quadratic interpolation methods continue to adhere to the predicted inverse proportionality. For bilinear interpolation, when $\Delta x \geq \pi\lambda_\mathrm{De}$, finite grid instability (FGI) is triggered,[30] leading to a deviation from the theoretical statistical noise behavior.

Finally, the average statistical noise produced by the three schemes exhibits an inverse proportionality to N_c, as shown in Fig. 5(c). The quantitative comparison provides direct evidence supporting the theoretical analysis: under identical conditions, the statistical noise in DGCA is approximately 87.5% of that in bilinear interpolation, as highlighted in Fig. 5(d). At the same N_c, the average noise level of DGCA is reduced to 83.2(1.2)%, in excellent agreement with theoretical predictions.

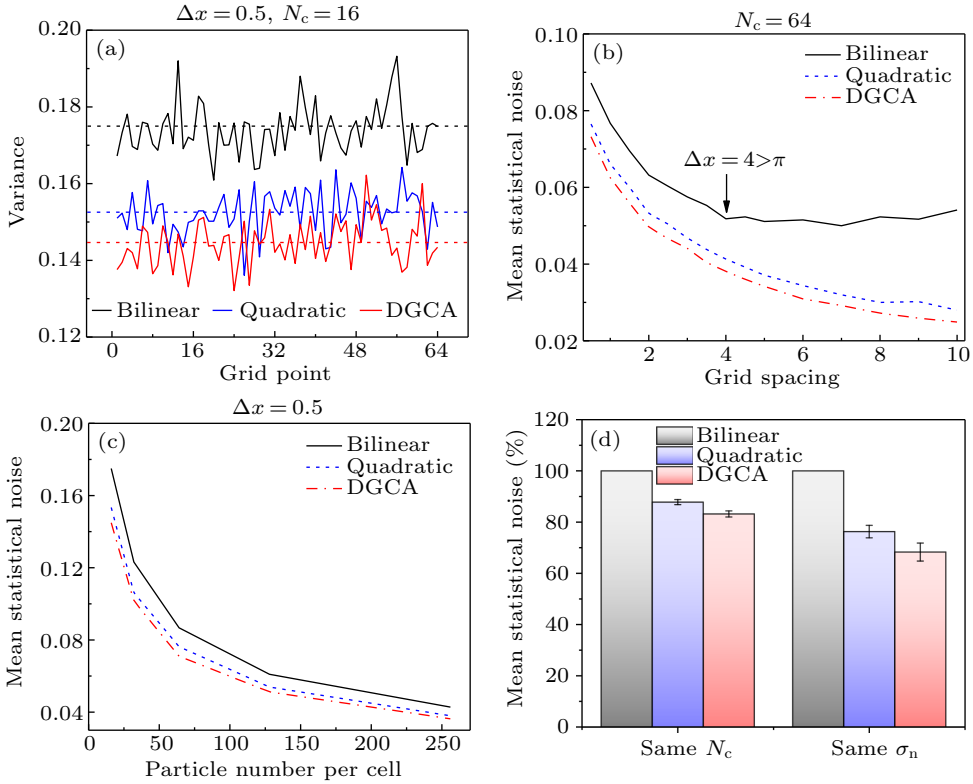


Fig. 5. Noise characteristics of the three charge deposition schemes. (a) Spatial distribution of the charge density variance, where bilinear, quadratic, and DGCA interpolations are denoted by black solid, blue solid, and red solid lines, respectively; the corresponding dashed lines of the same colors indicate their mean values. (b) Mean statistical noise as a function of grid spacing Δx. (c) Mean statistical noise as a function of the number of particles per cell N_c. (d) Relative values of quadratic interpolation and the DGCA scheme with respect to bilinear interpolation, obtained from panel (c). In panels (b) and (c), bilinear, quadratic, and DGCA interpolations are represented by black solid, blue dashed, and red dotted lines, respectively.

3.3. Energy conservation testing

Finally, we revisited the second experiment of electron motion in a stationary ion background, this time introducing a drift velocity of $u_0/\omega_p\Delta x = 0.1$ to the electron population.[31] Figure 6 shows the temporal evolution of the normalized energy change rate, defined as $e(t) = [E_{\text{total}}(t) - E_{\text{total}}(0)]/E_{\text{total}}(0)$, for the bilinear interpolation scheme as a function of N_c. Here, $E_{\text{total}} = E_f + E_{ke}$ denotes the conserved quantity, with the kinetic energy given by

$$E_{ke} = \frac{1}{2} m_p \sum v_p^2,$$

where the summation is performed over all particles. The simulation parameters are $N_g = 64$, $\Delta t = 0.1$, and $N_t = 1000$. The spatial resolution employed in the simulation is specified in the corresponding figure caption.

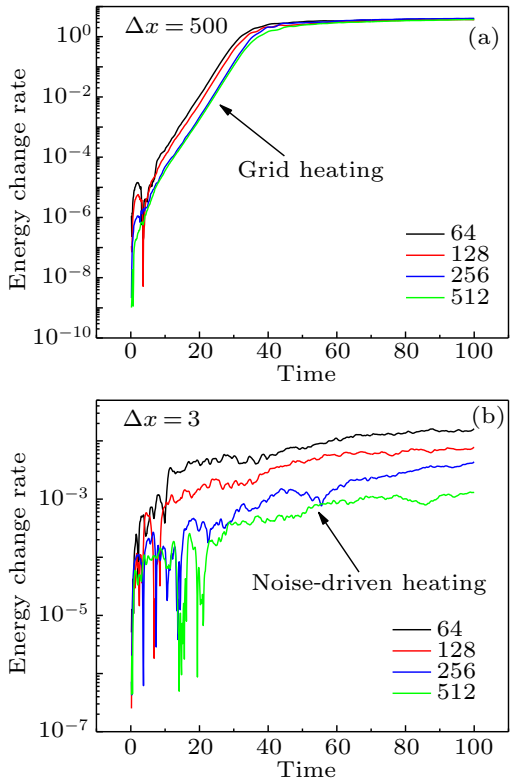


Fig. 6. Energy growth rate as a function of the number of particles per cell N_c at two spatial resolutions: (a) low resolution and (b) high resolution. The black, red, blue, and green solid lines correspond to increasing values of N_c. The results clearly distinguish two distinct mechanisms of numerical heating: grid heating and noise-driven heating.

Figure 6 distinctly reveals two separate heating mechanisms: grid heating and noise-driven heating,[32] when the grid spacing greatly exceeds the Debye length ($\Delta x = 500\lambda_{De}$), grid heating dominates. In this regime, the system exhibits exponential energy growth, with the total energy increasing by a factor of 2.5 within approximately 20 plasma periods, while remaining essentially independent of N_c. In contrast, at higher spatial resolution ($\Delta x = 3\lambda_{De}$), grid heating becomes negligible, and the energy evolution is primarily governed by statistical noise, which manifests as a gradual increase over tens of plasma periods. This noise-driven heating is progressively suppressed as N_c increases.

We conducted comparative analyses of the proposed method against both bilinear interpolation and quadratic schemes. The results are summarized in Fig. 7, with simulation parameters set to $N_g = 64$, $\Delta t = 0.1$, and $N_t = 1000$. The new method exhibits superior suppression of grid heating compared with the quadratic scheme, achieving both a lower heating rate and improved energy conservation [Fig. 7(a)]. Furthermore, the method effectively suppresses noise-driven heating, delivering a performance comparable to that of the quadratic interpolation [Fig. 7(b)]. These observations are consistent with the theoretical prediction of noise reduction in Subsection 2.3.

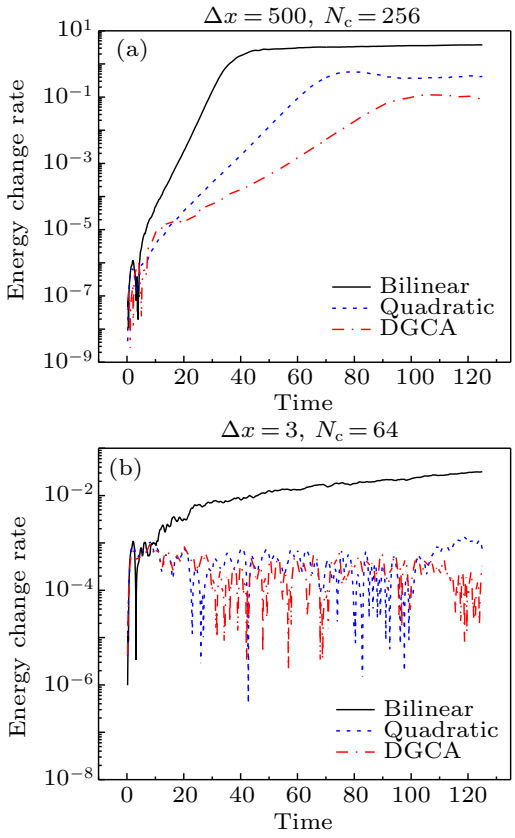


Fig. 7. Comparisons of energy conservation performance among the three methods. (a) Grid heating and (b) noise-driven heating. Bilinear, quadratic interpolations, and DGCA scheme are represented by the black solid, blue dashed, and red dotted lines, respectively. The proposed method demonstrates comparable suppression of noise-driven heating to that of quadratic interpolation, while exhibiting superior performance in mitigating grid heating.

We finally assessed the simulation accuracy of the three deposition schemes. Figure 8 presents the phase-space evolution, highlighting the manifestation of numerical heating, where the green line denotes the initial drift velocity u_0. Panels (a)–(c) correspond to results obtained with bilinear interpolation, quadratic interpolation, and the DGCA scheme, respectively. The simulation parameters are $\Delta x = 1$, $\Delta t = 0.1$, $N_g = 64$, $N_c = 256$, thermal velocity $v_{the} = 0$, and drift velocity $u_0 = 0.1$.

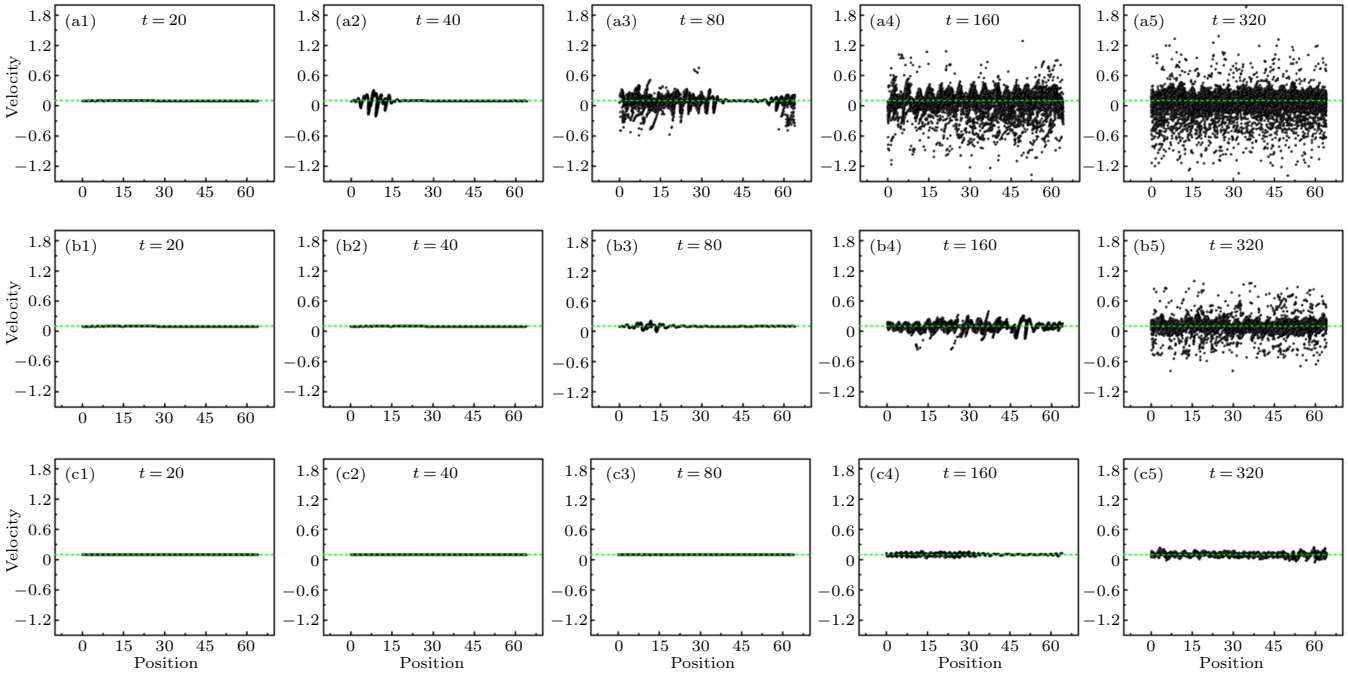


Fig. 8. Phase-space evolution obtained using (a) bilinear interpolation, (b) quadratic interpolation, and (c) the proposed DGCA scheme. The green line represents the theoretical distribution. Among the three methods, the DGCA scheme demonstrates the highest accuracy, yielding phase-space dynamics most consistent with the theoretical prediction.

For an ideal cold electron system without initial perturbations, the phase-space distribution is expected to remain a straight line. However, numerical heating inevitably introduces velocity perturbations, as evidenced in the simulation results. The bilinear interpolation scheme (Fig. 8(a)) exhibits pronounced numerical heating, with noticeable phase-space distortions emerging as early as $t = 40$. These distortions progressively intensify, ultimately leading to significant velocity broadening in the range from -1.5 to 2.0.

By contrast, the higher-order schemes demonstrate substantially improved performance. Although both the quadratic and DGCA schemes develop perturbations, they considerably delay the onset of numerical heating. The quadratic scheme shows visible distortions only at $t = 80$, whereas the DGCA scheme maintains a stable phase-space distribution until $t = 160$. Remarkably, even at $t = 320$, the DGCA scheme retains an almost linear phase-space structure, while the other two methods exhibit severe velocity divergence.

These results clearly highlight the superior numerical stability of the DGCA scheme, particularly in long-time simulations where numerical heating effects accumulate. The delayed onset and reduced magnitude of velocity perturbations demonstrate that DGCA more effectively preserves the kinetic integrity of the system.

4. Conclusions

In summary, we have introduced the dual-grid charge averaging (DGCA) deposition scheme, which operates through two fundamental steps: (i) independent charge deposition onto integer-grid nodes (native group) and half-grid points (mapped group, obtained via midpoint averaging), and (ii) computation of the final charge density as the weighted average of these two contributions. Within this framework, we derived an equivalent shape function for bilinear interpolation, expressed as a three-segment function with a support width spanning three grid cells, closely resembling a quadratic spline. A systematic analysis shows that the DGCA scheme reduces statistical noise to approximately 87.5% of that of bilinear interpolation, comparable to quadratic interpolation, thereby mitigating noise-driven heating. More importantly, DGCA demonstrates a marked advantage in suppressing aliasing, leading to a substantial reduction of grid heating. Collectively, these results indicate that DGCA effectively elevates bilinear interpolation to a higher-order formulation by virtue of its distinctive deposition mechanism.

Comprehensive numerical tests further validate the effectiveness of the proposed scheme. In Landau damping and two-stream instability cases, DGCA reproduces electric field energy evolution with high fidelity, confirming its accuracy in capturing fundamental plasma processes. In noise reduction and energy conservation tests, DGCA significantly suppresses numerical fluctuations and proves robust against both grid heating and noise-driven heating. While its noise suppression performance is comparable to quadratic interpolation, DGCA exhibits superior capability in controlling grid heating. Overall, DGCA achieves the highest simulation accuracy among the tested methods, as evidenced by phase-space diagnostics showing a delayed onset of numerical heating and final distributions closely aligned with theoretical predictions.

Looking forward, the key step in DGCA implementation

lies in constructing the equivalent shape function $S_{\mathrm{D}}(x)$, which provides a natural pathway for extending this methodology to electromagnetic PIC simulations. By employing charge-conserving current deposition functions,[33,34] and systematically mapping between integer and half-integer grid points, the DGCA framework can be generalized to current deposition. Furthermore, the equivalent shape function derived in this study offers an important perspective: DGCA transforms first-order (bilinear) interpolation into a higher-order form. While this function resembles but is not identical to the quadratic B-spline, it suggests the feasibility of developing a generalized iterative framework for constructing higher-order shape functions, which will be pursued in future work.

Acknowledgement

Project supported by the National Natural Science Foundation of China (Grant Nos. 12405237, 12405293, and 12305284).

References

[1] Zhang S J, Zhou W M, Yin Y, Zou D B, Zhao N, Xie D and Zhuo H B 2023 *Chin. Phys. B* **32** 035201
[2] Lehmann G and Spatschek K H 2024 *Phys. Rev. E* **110** 015209
[3] Yuan X X, Zhou C T, Zhang H, Li R, Ping Y L and Zhong J Y 2023 *Chin. Phys. B* **32** 054101
[4] Tonneau R, Pflug A and Lucas S 2020 *Plasma Sources Sci. Technol.* **29** 115007
[5] Kawamura E, Birdsall C K and Vahedi V 2000 *Plasma Sources Sci. Technol.* **9** 413
[6] Birdsall C K and Langdon A B 2005 *Plasma physics via computer simulation* (Taylor and Francis)
[7] Barnes D and Chacón L 2021 *Comput. Phys. Commun.* **258** 107560
[8] Acciarri M D, Moore C and Baalrud S D 2024 *Phys. Plasmas* **31** 093903
[9] Jubin S, Powis A T, Villafana W, Sydorenko D, Rauf S, Khrabrov A V, Sarwar S and Kaganovich I D 2024 *Phys. Plasmas* **31** 023902
[10] Arber T D, Bennett K, Brady C S, *et al.* 2015 *Plasma Phys. Control. Fusion* **57** 113001
[11] Brackbill J U 2016 *J. Comput. Phys.* **317** 405
[12] Filbet F and Sonnendrücker E 2003 *Numerical methods for the Vlasov equation, in: Numerical Mathematics and Advanced Applications* (USA: Springer)
[13] Ricketson L F and Cerfon A J 2017 *Plasma Phys. Control. Fusion* **59** 024002
[14] Deluzet F, Fubiani G, Garrigues L, Guillet C and Narski J 2022 *ESAIM: M2AN* **56** 1809
[15] Deluzet F, Fubiani G, Garrigues L, Guillet C and Narski J 2023 *J. Comput. Phys.* **480** 112022
[16] Evstatiev E G, Finn J M, Shadwick B A and Hengartner N 2021 *J. Comput. Phys.* **440** 110394
[17] Kawamura E, Birdsall C K and Vahedi V 2000 *Plasma Sources Sci. Technol.* **9** 413
[18] Fiuza F, Marti M, Fonseca R A, Silva L O, Tonge J, May J and Mori W B 2011 *Plasma Phys. Control. Fusion* **53** 074004
[19] Picklo M J, Tang Q, Zhang Y Z, Ryan J K and Tang X Z 2024 *J. Comput. Phys.* **502** 112790
[20] Faghihi D, Carey V, Michoski C, Hager R, Janhunen S, Chang C S and Moser R D 2020 *J. Comput. Phys.* **409** 109317
[21] Muralikrishnan S, Cerfon A J, Frey M, Ricketson L F and Adelmann A 2021 *J. Comput. Phys: X* **11** 100094
[22] Garrigues L, Tezenas du Montcel B, Fubiani G, Bertomeu F, Deluzet F and Narski J 2021 *J. Appl. Phys.* **129** 153303
[23] Garrigues L, Tezenas du Montcel B, Fubiani G and Reman B C G 2021 *J. Appl. Phys.* **129** 153304
[24] Guillet C 2024 *Multiscale Model Sim.* **22** 891
[25] Nicolas T, Dubois V, Fang Q and Lütjens H 2024 *Comput. Phys. Commun.* **299** 109151
[26] Verboncoeur J P 2005 *Plasma Phys. Control. Fusion* **47** A231
[27] Langdon A B, Cohen B I and Friedman A 1983 *J. Comput. Phys.* **51** 107
[28] Stix T 1992 *Waves in Plasmas* (New York, NY, USA: American Institute of Physics).
[29] Goldston R and Rutherford P 1995 *Introduction to plasma physics* (Taylor & Francis)
[30] Hockney W and Eastwood J W 1988 *Computer Simulation Using Particles* (CRC Press)
[31] Werner G R, Adams L C and Cary J R 2025 arXiv: 2503.05123v1
[32] Shadwick B A and Schroeder C B 2009 *AIP Conference Proceedings* **321** 1086
[33] Villasenor J and Buneman O 1992 *Comput. Phys. Commun.* **69** 306
[34] Esirkepov T Z H 2001 *Comput. Phys. Commun.* **135** 144